A&A 413, 241–249 (2004)
DOI: 10.1051/0004-6361:20031487

Astronomy
&
Astrophysics

Australia Telescope Compact Array imaging of circumstellar HCN line emission from R Scl

T. Wong[1], F. L. Schöier[2,3], M. Lindqvist[4], and H. Olofsson[3]

[1] CSIRO Australia Telescope National Facility, PO Box 76, Epping NSW 1710, Australia
[2] Sterrewacht Leiden, PO Box 9513, 2300 RA Leiden, The Netherlands
[3] Stockholm Observatory, AlbaNova, 106 91 Stockholm, Sweden
[4] Onsala Space Observatory, 439 92 Onsala, Sweden

Received 9 May 2003 / Accepted 19 September 2003

Abstract. We present radio-interferometric observations of HCN $J = 1 \rightarrow 0$ line emission from the carbon star R Scl, obtained with the interim 3-mm receivers of the Australia Telescope Compact Array. The emission is resolved into a central source with a Gaussian *FWHM* of $\sim 1''$, which we identify as the present mass loss envelope. Using a simple photodissociation model and constraints from single-dish HCN spectra, we argue that the present mass-loss rate is low, $\sim 2 \times 10^{-7}$ $M_\odot$ yr^{-1}, supporting the idea that R Scl had to experience a brief episode of intense mass loss in order to produce the detached CO shell at $\sim 10''$ radius inferred from single-dish observations. Detailed radiative transfer modelling yields an abundance of HCN relative to H_2, $f_{\rm HCN}$, of $\sim 10^{-5}$ in the present-day wind. There appears to be a discrepancy between model results obtained with higher transition single-dish data included and those from the $J = 1 \rightarrow 0$ interferometer data alone, in that the interferometer data suggest a smaller envelope size and larger HCN abundance than the single-dish data. The lack of HCN in the detached shell, $f_{\rm HCN} \lesssim 2 \times 10^{-7}$, is consistent with the rapid photodissociation of HCN into CN as it expands away from the star.

Key words. circumstellar matter – stars: carbon – stars: AGB and post-AGB – stars: mass-loss

1. Introduction

In the late stages of asymptotic giant branch (AGB) evolution, material is ejected via a slow (5–30 km s^{-1}) stellar wind into a circumstellar envelope of gas and dust. This mass loss (on the order of 10^{-7}–10^{-5} $M_\odot$ yr^{-1}) is a key process for enriching and replenishing the interstellar medium, yet the mechanisms by which it occurs are not understood in detail. In particular, there is evidence that strong variations in the mass loss rate, perhaps related to flashes of helium shell burning, can lead to the formation of circumstellar detached shells (Olofsson et al. 1990). Such shells can be inferred from their excess emission at long infrared wavelengths (due to a lack of hot dust close to the star, Willems & de Jong 1988) and confirmed by a ring-like morphology in maps of dust or CO line emission.

Detached shells have been observed around about a half-dozen AGB stars (see review by Wallerstein & Knapp 1998), but only U Cam (Lindqvist et al. 1996, 1999) and TT Cyg (Olofsson et al. 1998, 2000) have been mapped with millimetre-wave interferometers. Both cases reveal a beautifully symmetric shell showing uniform expansion from the star. High-resolution molecular line observations offer the possibility not only to confirm detachment, but also to study variations in mass loss on short (<100 yr) timescales, related to the shell thickness, and to look for departures from spherical symmetry.

As one of the initial targets for the 3-mm receiver systems being installed on the Australia Telescope Compact Array (ATCA), we have imaged the HCN $J = 1 \rightarrow 0$ emission from the carbon star R Sculptoris (R Scl). Previous observations by Olofsson et al. (1996) with the Swedish-ESO Submillimetre Telescope (SEST) have indicated a detached shell which is only marginally resolved (radius $\approx 10''$) in the CO $J = 3 \rightarrow 2$ line, suggesting a relatively young age for the shell ($\lesssim 10^3$ yr, using the observed shell expansion velocity of 16.5 km s^{-1} and a distance of 360 pc; Schöier & Olofsson 2001). Detections of other molecules like HCN, CS, and CN have also been reported by Olofsson et al. (1996). These molecules are more easily photodissociated than CO, but it is not clear whether they are located in the detached shell or confined to the current mass loss envelope, which the SEST data, with limited spatial resolution, could not distinguish from the shell. Another outstanding question is the relationship between the molecular gas shell and the larger dust shell (radius $\approx 20''$) seen in scattered optical light (González Delgado et al. 2001; González Delgado et al. 2003). The recent commissioning of a southern millimetre array motivated us to obtain much higher resolution data toward this object.

Send offprint requests to: T. Wong, e-mail: `Tony.Wong@csiro.au`

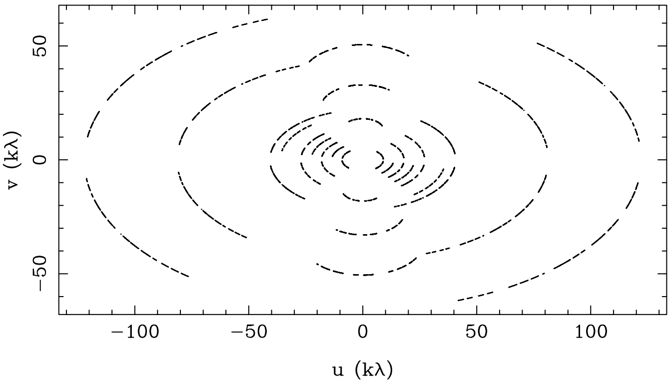

Fig. 1. Coverage of the visibility plane obtained after combining observations in all four ATCA configurations (EW214, EW352, H168, and 750A).

In this paper we present the results of our ATCA observations and analyse them, along with new and previously published single-dish spectra, using a detailed radiative transfer code for modelling circumstellar line emission (Lindqvist et al. 2000; Schöier & Olofsson 2001).

2. Observations and data reduction

2.1. Interferometer data

At the time of the observations, the ATCA had three antennas of 22 m diameter equipped with dual polarisation 3-mm receivers covering the bands 84.9–87.3 and 88.5–91.3 GHz. We observed R Scl between 2002 June and October in four different array configurations: EW214 (baselines of 31, 61, and 92 m), EW352 (46, 77, and 122 m), H168 (61, 111, and 171 m), and 750A (138, 275, and 413 m). Note that in the H168 configuration, the 3-mm antennas are situated in a north-south line; the remaining configurations are east-west arrays. The 750A observations were taken over two nights spaced 3 days apart; observations in the other configurations occurred on single nights. The combined visibility plane coverage is shown in Fig. 1.

All observations were conducted in mostly clear weather, with above-atmosphere single-sideband system temperatures of $T^*_{\rm sys} \approx 300$ K near the zenith. The correlator was configured to receive both linear polarisations in two frequency windows: a narrowband (spectral line) window centred on the HCN $J = 1 \rightarrow 0$ line at 88.6 GHz with 128 channels across 32 MHz, and a wideband (continuum) window centred at 89 GHz with 32 channels across 128 MHz. The pointing and phase centre was at $\alpha_{2000} = 01^{\rm h}26^{\rm m}58\overset{\rm s}{.}49$, $\delta_{2000} = -32°32'35\overset{''}{.}5$, which is 5″ east of the stellar position (in the subsequent data analysis we have applied an offset so that the phase centre coincides with the star). At 89 GHz the ATCA primary beam has a $FWHM$ of about 35″.

Gain calibration was performed by frequent observations (every 10−20 min) of the nearby quasars B0104−408 or B0208−512. The amplitude and phase gains were derived using the continuum window data and then transferred to the spectral line window after applying offsets determined from a half-hour integration on the bandpass calibrator (B1921−293, B2255−282, or B0420−014). Channel-dependent gains were also determined from the bandpass calibrator. Uranus was used to set the flux scale, assuming a uniform disk with brightness temperature of 134 K. We also adjusted the antenna pointing once an hour on B0208−512; typical pointing shifts were ∼5″.

All data processing was conducted using the MIRIAD package. As an initial step in the reduction, values of $T^*_{\rm sys}$ measured via the chopper wheel method (Kutner & Ulich 1981) were used to rescale the data, then an elevation-dependent gain curve was applied based on observations of an SiO maser taken on 2002 June 4. Subsequent processing was as described above using standard routines. The calibrated visibilities were Fourier transformed using robust weighting and a $0\overset{''}{.}5$ pixel size with a channel spacing of 1 km s^{-1} (roughly the effective velocity resolution given the original channel spacing of 0.25 MHz ≈ 0.8 km s^{-1}). The maps were then cleaned down to a 2σ level over the inner 20″ × 20″.

Over the course of the observations, it became clear that there were residual phase errors in the data that were not being removed by the standard technique of phase referencing off a nearby quasar. These phase errors, revealed as phase jumps when switching sources, can be modelled as errors in the antenna positions of up to a few mm. For most of the data, we were able to minimise the effects of these phase errors by refining the baseline solution from observations of multiple quasars taken on the same or adjacent days. No such correction could be applied to the EW352 data, which are therefore excluded from the image analysis below (Sect. 3.1), but are included in the visibility analysis after self-calibration (Sect. 3.3).

2.2. Single-dish data

As a complement to the interferometer observations, multi-transition single-dish data have been obtained. The single-dish data are used to check that the interferometer recovers all of the source flux and also to constrain the circumstellar HCN models. Using the SEST, the HCN $J = 1 \rightarrow 0$ and $J = 3 \rightarrow 2$ transitions were observed in February 2003 and December 1996 respectively. Two acousto-optical spectrometers were used at SEST (86 MHz bandwidth with 43 kHz channel separation, and 1 GHz bandwidth with 0.7 MHz channel separation). Dual beam switching (beam throws of about 11′), in which the source was placed alternately in the two beams, was used to eliminate baseline ripples. The line intensities are given in the main beam brightness temperature scale ($T_{\rm mb}$), i.e., the antenna temperature has been corrected for atmospheric attenuation (using the chopper wheel method) and divided by the main beam efficiency. In addition, recently published HCN $J = 3 \rightarrow 2$ and $J = 4 \rightarrow 3$ spectra from Bieging (2001), obtained with the Heinrich Hertz Submillimeter Telescope (HHT), have been used. The single-dish data are presented in Table 1 and Sect. 4.2.

3. Observational results

3.1. Channel maps

Figure 2 shows the HCN $J = 1 \rightarrow 0$ channel maps (with the EW352 data excluded) binned into 2 km s^{-1} channels.

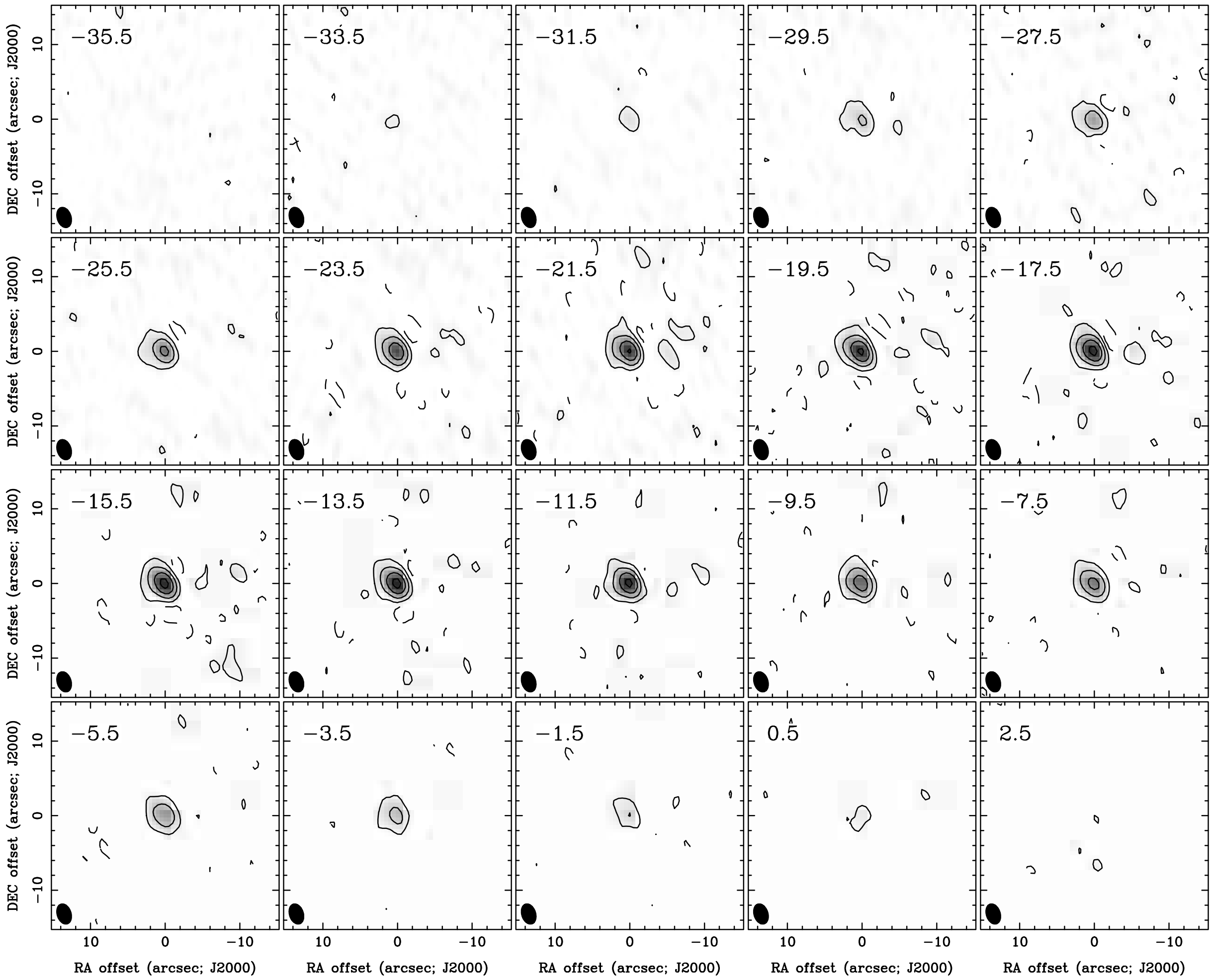

Fig. 2. Deconvolved channel maps of HCN emission from R Scl. The contour levels are $0.05n^2$ Jy beam^{-1}, where $n = 1, 2, 3, 4$, and the beam size is 2.″7 × 1.″8. The velocity channels (given in the LSR frame) have been binned to 2 km s^{-1}.

Table 1. Single-dish HCN molecular line observations of R Scl.

Trans.	Tel.	$\int T_{\rm mb} {\rm d}V^a$ [K km s^{-1}]	$T_{\rm mb}{}^b$ [K]	$FWHM^b$ [km s^{-1}]	$V_\star{}^b$ [km s^{-1}]
$J = 1 \rightarrow 0$	SEST	1.6	0.08	19.7	−16.2
$J = 3 \rightarrow 2$	SEST	5.4	0.36	14.6	−17.4
$J = 3 \rightarrow 2$	HHT^c	2.4	0.13	16.1	−18.5
$J = 4 \rightarrow 3$	HHT^c	4.1	0.29	14.8	−17.7

[a] Total integrated intensity calculated over full extent of line.
[b] Estimated from a Gaussian fit to the observed spectrum.
[c] From Bieging (2001).

The synthesised beam is 2.″7 × 1.″8 with a position angle of 18°. The rms noise in the 1 km s^{-1} channel maps is σ = 23 mJy beam^{-1}; the peak emission reaches a level of about 40σ. We note here that the HCN $J = 1 \rightarrow 0$ line actually consists of three hyperfine components of relative strength 3:5:1 (in order of increasing frequency), with the low-frequency satellite line shifted +4.8 km s^{-1} and the high-frequency satellite line shifted −7.1 km s^{-1} with respect to the main line.

Inspection of the channel maps suggests that the source is moderately resolved, a result which is confirmed by the visibility analysis in Sect. 3.3. The source also appears to be somewhat extended to the east. We believe that this extension is most likely attributable to the instrumental phase errors discussed in Sect. 2.1: mapping the EW214 data alone shows the emission to be displaced by about 0.″6–0.″7 to the east of the star's position, whereas the other tracks do not show such an offset. The phase error needed to produce such an offset is ~30°, which is within the range expected from residual errors in the baseline solution.

Fitting two-dimensional Gaussians to the individual channel maps, we find no systematic variations in source size or position angle with velocity. Across the peak of the line profile, from −10 to −20 km s^{-1}, the average values of the major and minor axis $FWHM$ are 3.″1 and 2.″3 respectively, with a position angle of 36° (note that the beam has not been deconvolved from these values).

We see no indication of an expanding shell structure corresponding to that seen in the SEST CO $J = 3 \rightarrow 2$ data. A shell

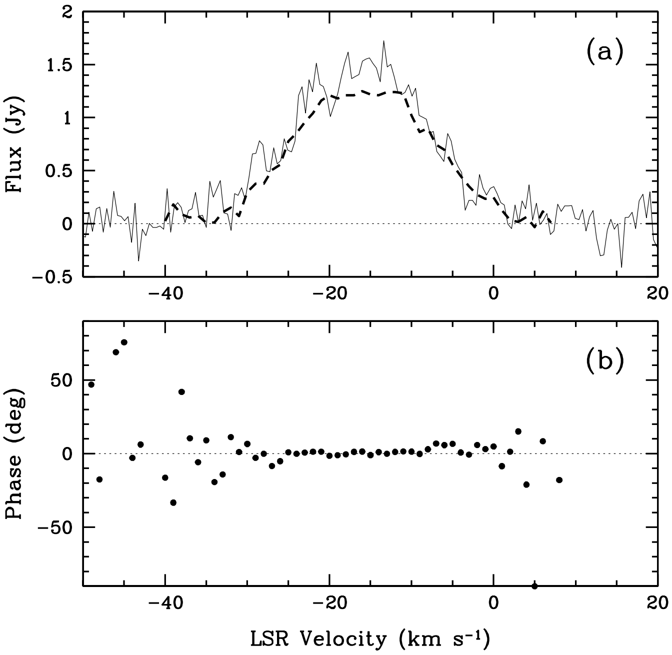

Fig. 3. a) HCN (1–0) spectra for R Scl, with the dashed line derived from the ATCA image (integrating the channel maps over a 6″ × 6″ box centred on $\alpha_{2000} = 01^h26^m58\fs09$, $\delta_{2000} = -32°32'35\farcs5$) and the thin solid line from the SEST observations. **b)** Average visibility phase spectrum, including data from all baselines and array configurations. The phase vs. time has been self-calibrated to bring the average phase to 0°.

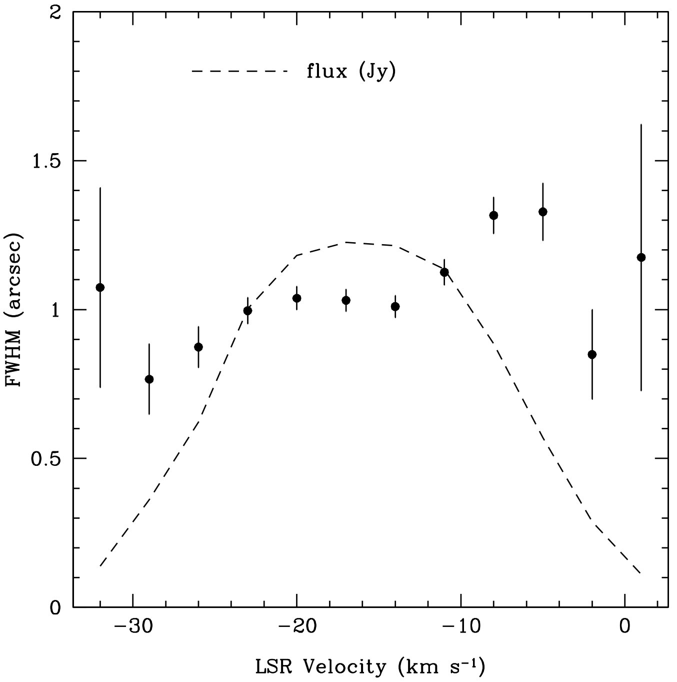

Fig. 4. *FWHM* of axisymmetric Gaussian fits to the visibility data averaged in 3 km s^{-1} channels. The source is constrained to lie at the phase centre. The flux of the model Gaussian, on the same numerical scale but in Jy, is overplotted as a dashed line.

of radius 10″ would appear well within the half-power radius of the primary beam, especially on the eastern side, since the pointing centre was offset 5″ east of the star. Moreover, an *expanding* spherical shell would become smaller near the extreme velocities (aside from some complications due to the hyperfine structure of the HCN line), and thus certainly fall within the primary beam, yet there is no indication that the source structure or size changes with velocity.

3.2. Spectra

The integrated HCN $J = 1 \rightarrow 0$ ATCA spectrum is shown in Fig. 3a, overlaid on the equivalent SEST spectrum. A Gaussian fit to the ATCA spectrum gives a mean velocity, $V_\star$, of −15.8 km s^{-1} and a *FWHM* of 19.1 km s^{-1}; however, this may be affected by the hyperfine structure of the HCN line. The peak flux of 1.2 Jy agrees, within the calibration uncertainties, with the single-dish flux of 1.4 Jy detected with the SEST ($S = \eta_B T_{\rm mb} \Gamma^{-1}$, where $\eta_B = 0.75$, $T_{\rm mb} = 75$ mK, and $\Gamma^{-1} = 25$ Jy K^{-1}). Thus, our lack of interferometer spacings less than 30 m does not appear to have resulted in a significant amount of "missed" flux, at least within the 58″ SEST beam. This confirms that virtually all of the HCN emission comes from the central component.

The higher-transition spectra taken with the SEST and HHT (see Table 1) are in general agreement with the $J = 1 \rightarrow 0$ spectra, except that their mean velocity is ≈−17.5 km s^{-1} and the linewidths are somewhat narrower, *FWHM* ≈ 15 km s^{-1}. Since these lines are less affected by hyperfine structure, they should serve as a better indication of the kinematics of the envelope. The spectra are presented and discussed in Sect. 4.2.

3.3. Visibility analysis

The results of Sect. 3.1 indicate that the HCN $J = 1 \rightarrow 0$ emission comes from a compact central source that is only moderately resolved by our observations. We now proceed to analyse the visibilities directly, under the assumption that the emission structure is axisymmetric, i.e. there is no phase information in the visibilities. This assumption allows us to self-calibrate the data in phase (in practice a 30-min interval was used) and therefore include the EW352 data, which were strongly affected by phase errors. We stress that applying self-calibration with only three interferometer baselines is guaranteed to produce an axially symmetric source at the phase centre, as long as closure errors are negligible. Independent evidence that there is little additional source structure comes from the averaged visibility phase spectrum shown in Fig. 3b. Since the channel-to-channel phase has *not* been self-calibrated, but only calibrated using the bandpass calibrator, the flatness of the phase spectrum indicates that the source structure is the same at all velocities.

We fit a model of an axisymmetric Gaussian to the self-calibrated visibilities. The resulting *FWHM* in arcseconds is plotted in Fig. 4, along with the flux of the model. Most of the values are close to $1\farcs0$, although somewhat higher values ($1\farcs3$) are seen at the redshifted edge of the line. An average over all points gives $1\farcs05 \pm 0\farcs17$. Note that a *FWHM* of 1″ corresponds to a radius at half maximum, at the distance of R Scl, of about 200 AU (3×10^{15} cm). As with the image analysis in

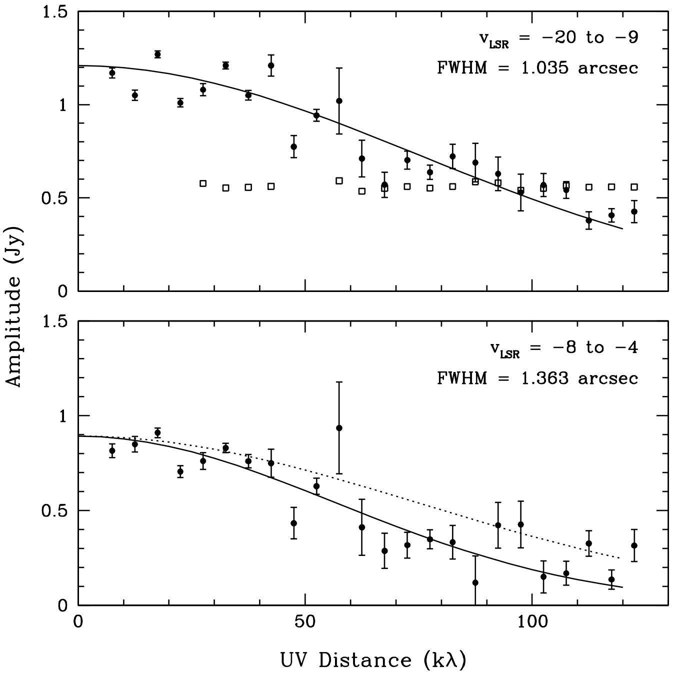

Fig. 5. *(Top)* Averaged visibility amplitudes, in 5 kλ bins, across the peak of the line profile (filled circles). The solid line is the model fit, with a *FWHM* of 1.″0. The open squares represent the averaged visibility amplitudes of the gain calibrator, B0104−408. *(Bottom)* Same but for the high-velocity edge of the line profile. The solid line is the model fit, with a *FWHM* of 1.″4, whereas the dotted line corresponds to a *FWHM* of 1.″0.

Sect. 3.1, we do not see the variation in size with line-of-sight velocity expected for an expanding shell.

The top panel of Fig. 5 shows a 1.″0 Gaussian model fit to the peak of the line profile, overlaid on the visibility amplitude averaged in 5 kλ bins. For comparison, the open squares give the average visibility amplitude for the phase calibrator, B0104−408, during the two October runs in 750A (the amplitude was ~30% lower in the June runs, but this may be due to intrinsic variability of this quasar and/or errors in relative flux calibration). Note that the amplitude of the calibrator does not show a significant decrease with baseline length, as would be expected if atmospheric phase decorrelation were affecting the averaged visibility amplitudes. Consequently, there is no doubt that the HCN emission from R Scl has been spatially resolved by our observations. However, because our baselines are not long enough to show a possible null in the visibility function, other types of extended models besides a Gaussian (e.g., a uniform disk or optically thin sphere) are not excluded.

The bottom panel of Fig. 5 shows a 1.″36 Gaussian model fit to the redshifted edge of the line profile, which showed indications of a larger source size in Fig. 4. While the fit appears to be a reasonable one, there are clearly some bins that agree better with the 1″ source size derived from the full velocity range (dotted line). Thus, the significance of the larger source size at these velocities appears doubtful. We note that for an expanding shell that has been well-resolved, we would expect the source size to decrease, rather than increase, near the line wings.

4. Radiative transfer modelling

To model the circumstellar line emission we have used a detailed non-LTE radiative transfer code, based on the Monte Carlo method (Bernes 1979). The code has been described in detail in Schöier (2000) and Schöier & Olofsson (2001) and has been benchmarked against a wide variety of molecular line radiative transfer codes in van Zadelhoff et al. (2002). The code assumes a spherical envelope expanding at constant velocity and includes radiative excitation through vibrationally excited states, and a full treatment of line overlaps between various hyperfine components. Our procedure and the relevant molecular data are summarised in Lindqvist et al. (2000).

From the HCN line emission alone it is not possible to constrain both the abundance of HCN (relative to H_2) and the mass loss rate. For our analysis, therefore, we first adopt a mass loss rate for the present day wind. We construct a model of the CO envelope to derive the temperature profile, then determine the best-fit values for the HCN abundance and envelope size, using both the single-dish and interferometer data as constraints. The HCN abundance, f_{HCN}, is taken to be fixed throughout the envelope out to a specified outer radius, r_{HCN}.

4.1. The mass loss rate and temperature profile

Le Bertre (1997) estimated the present mass loss rate for R Scl to be approximately 10^{-7} $M_\odot$ yr^{-1}, scaled to our adopted distance of 360 pc, based on radiative transfer modelling of the observed dust emission. This method assumes that the dust grain properties and the dust-to-gas mass and velocity ratios in R Scl are the same as in IRC+10216, for which the mass loss rate is taken to be 2.5×10^{-5} $M_\odot$ yr^{-1} at a distance of 200 pc. A larger mass loss rate of 4×10^{-7} $M_\odot$ yr^{-1} (again scaled to our adopted distance) is derived by Gustafsson et al. (1997), using K I scattered light observations, but this estimate must be considered relatively uncertain since it is based on a method which has not been extensively tested. As long as the size of the emitting region is limited by photodissociation rather than excitation, a rough estimate of the mass loss rate can also be obtained from the observed size of the HCN brightness distribution, using a simple photodissociation model (cf., Lindqvist et al. 2000). For an estimated expansion velocity of 10.5 km s^{-1} (see below), a mass loss rate of approximately 5×10^{-7} $M_\odot$ yr^{-1} is derived assuming the same dust properties as for IRC+10216 (Schöier & Olofsson 2001). Based on these estimates, we adopt a mass loss rate of 2×10^{-7} $M_\odot$ yr^{-1} for the present epoch. Thus, the mass loss rate for R Scl appears higher than the present mass loss rates of sources with relatively old detached shells like TT Cyg ($\dot{M}$ ~ 3×10^{-8} $M_\odot$ yr^{-1}; Olofsson et al. 1998, 2000) but comparable to that of the "young shell" source U Cam ($\dot{M}$ ~ 2.5×10^{-7} $M_\odot$ yr^{-1}; Lindqvist et al. 1996, 1999).

The expansion velocity of the wind is a free parameter in the radiative transfer that is well constrained by the width of the observed lines. A value of 10.5 km s^{-1} can reproduce both the $J = 1 \rightarrow 0$ line and the higher J transition HCN line profiles, which are much less affected by hyperfine structure (see Sect. 4.2). The source is assumed to have a distance of 360 pc and the stellar radiation to be described by a blackbody with a luminosity of 5500 $L_\odot$ and a temperature of 2500 K (Schöier & Olofsson 2001; Kerschbaum, priv. comm.). The inner radius of the envelope is fixed at 3×10^{14} cm (20 AU).

Using the above parameters we have computed a CO model of the envelope, adopting a CO abundance of 1×10^{-3} relative to H_2. The outer radius of the CO envelope, $\sim 3 \times 10^{16}$ cm (6″), is obtained from a CO photodissociation model (Mamon et al. 1988). In addition to determining the steady-state level populations of the CO molecule, the code simultaneously solves the energy balance equation, including the most relevant heating and cooling processes. Heating is dominated by collisions between the dust and gas, while cooling is generally dominated by CO line emission, although adiabatic cooling due to the expansion of the envelope is also important. We have assumed that R Scl has the same dust properties as IRC+10216. Our excitation analysis allows for a self-consistent treatment of molecular line cooling. In this way the kinetic temperature structure of the envelope is determined, for use in the subsequent HCN line modelling. Throughout most of the envelope the temperature structure is well described, to within 10%, by a simple power-law $T_{\rm kin} = T_0(r_0/r)^{0.47}$, where $T_0 = 182$ K and $r_0 = 1 \times 10^{16}$ cm. However, in the inner parts of the envelope ($r \leq 1 \times 10^{15}$ cm) the temperature rises more dramatically to a value of 1350 K at the inner edge of the envelope.

We find that our derived CO line intensities are much lower than the observed ones, consistent with most of the observed CO line emission coming from a detached shell distinct from the present mass loss envelope. A more thorough discussion will be presented in Lindqvist et al. (in prep.).

4.2. HCN line modelling

With the physical structure of the envelope fixed, a set of models was calculated where the HCN abundance relative to H_2, $f_{\rm HCN}$, was allowed to vary from 5×10^{-6} to 5×10^{-5} and the outer radius of the HCN-emitting envelope from 2×10^{15} cm to 5×10^{16} cm. For each model a total χ^2 (for a definition see Schöier & Olofsson 2001) was determined via comparison with the observed spectra, assuming a calibration uncertainty of 20% for each spectrum. In addition to the single-dish data presented in Table 1, the ATCA spectrum at the centre pixel of the maps was used in the χ^2 analysis. Note that the χ^2 map (Fig. 6) shows that the line intensities become relatively insensitive to the adopted size of the HCN envelope when $\gtrsim 3 \times 10^{16}$ cm. This is where the emitting region becomes excitation limited. Such solutions, however, are implausible given that the CO envelope is calculated to extend only to 3×10^{16} cm, and CO is less readily photodissociated than HCN. The best fit model has an abundance of $(1.2 \pm 0.4) \times 10^{-5}$ and a size of $(1.4 \pm 0.5) \times 10^{16}$ cm (Fig. 6; Model 1). The reduced χ^2 has a value of 1.3, indicating a good fit. However, as can be seen by comparing this model with the observed spectra (Fig. 7), the model ATCA spectrum is too weak and presents more of a double-peaked rather than parabolic line shape. Note that we have not included the vibrationally excited lines seen in the $J = 3 \rightarrow 2$ and $J = 4 \rightarrow 3$ spectra in Fig. 7 in our analysis, given that they are masing and highly variable (Bieging 2001).

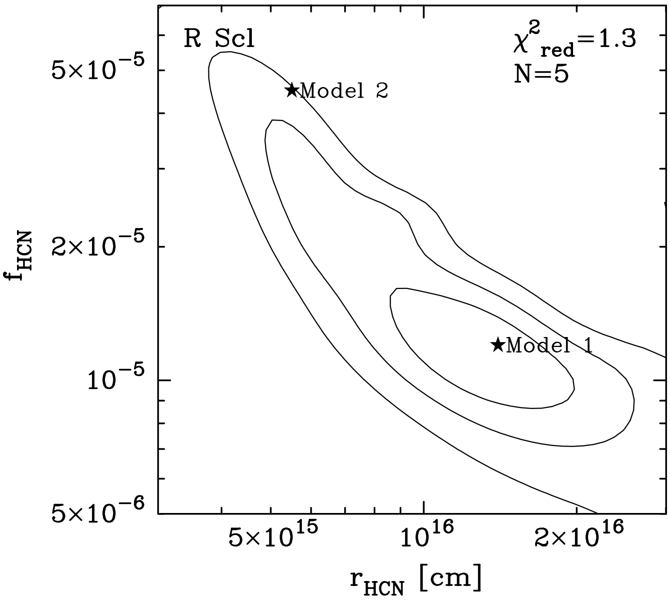

Fig. 6. χ^2 map showing the sensitivity of the HCN envelope model to the adjustable parameters $f_{\rm HCN}$ and $r_{\rm HCN}$. Contours are drawn at $\chi^2_{\rm min}$ + (2.3, 6.2, 11.8) indicating the 68% ("1σ"), 95% ("2σ"), and 99.7% ("3σ") confidence levels, respectively. The quality of the best fit model (Model 1) can be estimated from the reduced chi-squared statistic $\chi^2_{\rm red} = \chi^2_{\rm min}/(N{-}2)$, and is shown in the upper right corner. Also shown is the number of observational constraints used, N, which includes the single-dish spectra and the ATCA spectrum at the centre pixel. The model that best reproduces the visibility amplitudes obtained by ATCA (Model 2) is also shown for comparison.

The main source of the discrepancy between our model and the ATCA data is that the size of the model envelope is approximately five times larger than that obtained from the interferometer uv-plane data (Sect. 3.3). Applying the ATCA uv sampling to the model envelope, we find that the model severely underpredicts the flux observed on long baselines (Fig. 8). As shown by the dashed line, a better fit is obtained by raising the abundance of HCN ($f_{\rm HCN} = 4.5 \times 10^{-5}$) while making the envelope smaller ($r_{\rm HCN} = 5.5 \times 10^{15}$ cm) (Model 2). However, such a model would predict much stronger emission (by ∼50%) in the higher J transitions, in conflict with the single-dish constraints (Fig. 6). We also note that Model 2 predicts a decrease in source size at the extreme velocities of the line profile, which, while expected for a spherically symmetric wind expanding at a constant velocity, is not evident in the observations (Fig. 4).

It is not clear how to resolve the discrepancy between the modelling and data. Changing the adopted mass loss rate affects the HCN abundance but not, to a first approximation, the HCN envelope size. Since the HCN lines are mostly radiatively excited, mainly through the 3-μm stretching mode which lies close to the peak of the spectral energy distribution, changing the kinetic temperature structure within reasonable limits also does not significantly affect the model results. While the HCN $J = 1 \rightarrow 0$ hyperfine lines can be inverted in parts of the envelope, the effect of maser emission on the scales observed here ($\gtrsim 1''$) should be small. Previous modelling of $H^{12}CN$ and

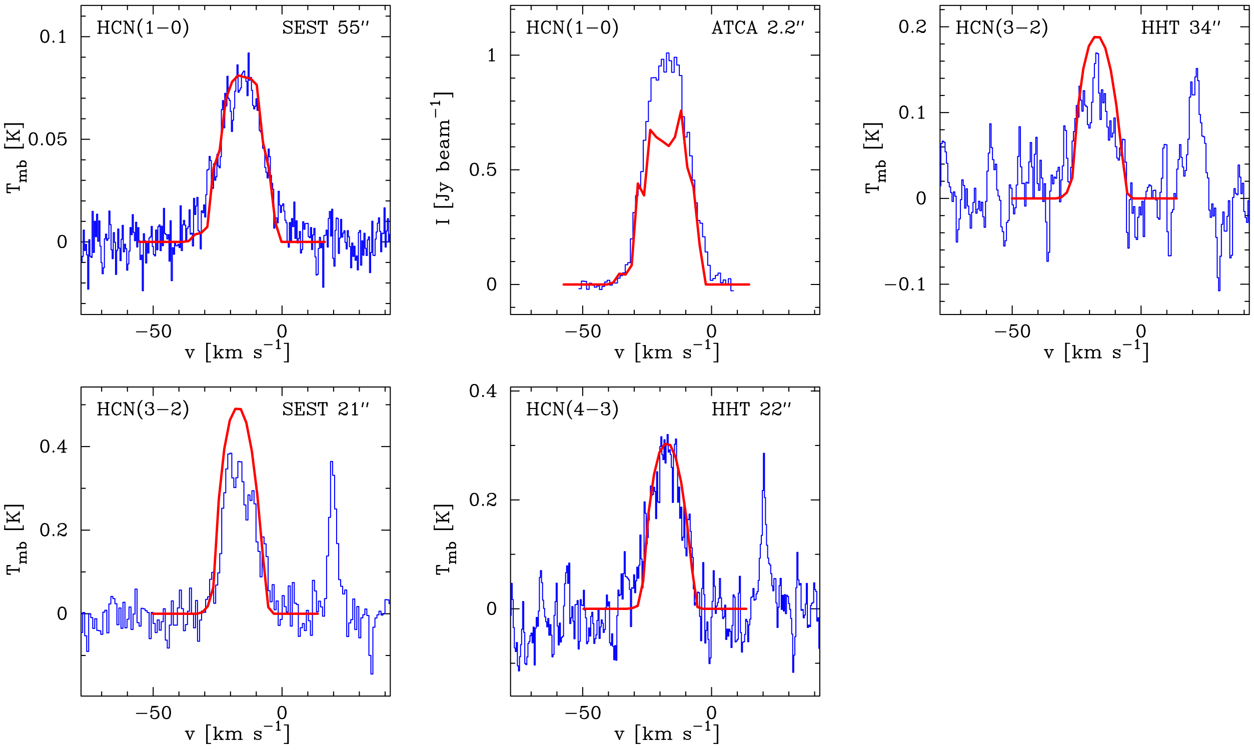

Fig. 7. Best fit model (full line), using a HCN abundance of 1.2×10^{-5} and envelope size of 1.4×10^{16} cm, overlaid on the observed spectra (histograms). The narrow spectral features in the $J = 3 \rightarrow 2$ and $J = 4 \rightarrow 3$ spectra are from vibrationally excited HCN. The ATCA spectrum is taken at the centre pixel of the image cube.

$H^{13}CN$ data for a sample of carbon stars by Lindqvist et al. (2000) indicates that our technique may be less successful at modelling lines of high optical depth such as HCN, where changes in the physical parameters in the envelope, such as density structure and velocity field, will have large effects.

A higher degree of sophistication in the modelling would require more detailed observations. The near-term prospect of higher resolution HCN $J = 1 \rightarrow 0$ observations is remote, but higher resolution mapping of other molecules (such as CO and CN) would be useful. In particular, good spatial resolution will be important in order to address the possibility that the medium is highly clumped, as has been suggested by Olofsson et al. (1996).

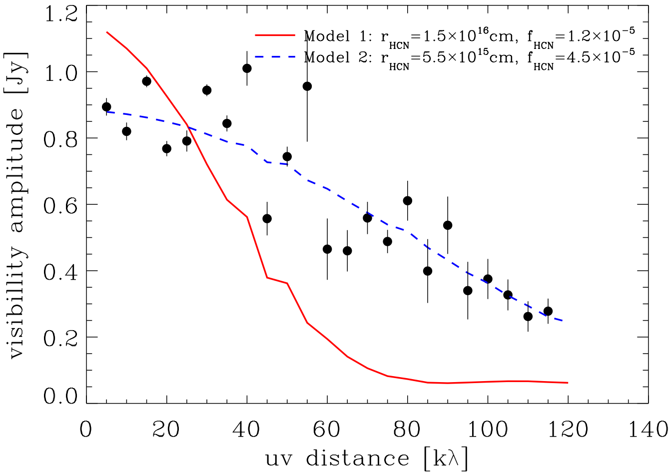

Fig. 8. Visibility amplitudes of the observed HCN $J = 1 \rightarrow 0$ line emission obtained at ATCA towards R Scl as a function of the projected baseline length. The observations, integrated from −28 to −4 km s^{-1} and binned to 5 kλ, are plotted as filled symbols with 1σ error bars. Also shown is the result of applying the same *uv* sampling to the best-fit circumstellar model including the single-dish data (Model 1; solid line). A model with higher abundance and smaller envelope size is able to reproduce the interferometer observations much better (Model 2; dashed line).

5. Discussion: The detached shell

Since our HCN data do not show direct evidence for a detached shell around R Scl, it is worth reviewing the evidence that such a shell exists. First there are the far-infrared colours of this star, which are similar to those of stars with clearly detached envelopes (Olofsson et al. 1990). In addition, the CO $J = 3 \rightarrow 2$ SEST maps presented by Olofsson et al. (1996), with an effective resolution of about 7″, show the systematic change in source size with velocity expected from an expanding spherical shell, as well as off-centre peaks in the central velocity channels that are indicative of detachment. Third, as discussed by González Delgado et al. (2003), attempts to model the CO data with only a continuous mass loss envelope lead to very high mass loss rates (∼10^{-5} $M_\odot$ yr^{-1}), which cannot be reconciled with the double-peaked line profile nor produce the extended brightness distribution of the CO $J = 3 \rightarrow 2$ line. A high mass loss rate is also inconsistent with the fact that the star is optically bright. Finally, the detection of a geometrically thin dust shell in polarised optical light is also noteworthy

(González Delgado et al. 2003), although this shell appears to have a radius roughly twice as large as that of the proposed CO shell.

The modelling presented in this paper provides indirect support for the hypothesis that R Scl has experienced a brief episode of intense mass loss, leading to the formation of a detached CO-emitting shell. Our derived HCN abundance of about 1×10^{-5} is in excellent agreement with the estimated photospheric HCN abundance of $\sim 8 \times 10^{-6}$ for R Scl determined by Olofsson et al. (1993). It is also roughly consistent with the abundances of $\sim 5 \times 10^{-5}$ obtained by Lindqvist et al. (2000) for a small sample of carbon stars. Since for a given line intensity the derived abundance scales inversely with the mass loss rate (Olofsson et al. 1993), this argues in favour of our adopted mass loss rate of 2×10^{-7} $M_\odot$ yr^{-1}, which is two orders of magnitude lower than the mass loss rate needed to model the CO emission (Lindqvist et al., in prep.). Furthermore, as noted already by Olofsson et al. (1996), the HCN expansion velocity of 10.5 km s^{-1} is significantly lower than that of 16.5 km s^{-1} measured from the CO lines. The fact that the "attached" (present mass loss) envelope expands more slowly than the detached shell is even more pronounced in sources with old detached shells, e.g. TT Cyg (Olofsson et al. 1998, 2000), where expansion velocities for the attached envelope as low as 4 km s^{-1} has been measured. R Scl is more reminiscent of U Cam (Lindqvist et al. 1996, 1999), which has a relatively young detached shell, and whose attached envelope expands more slowly than the detached shell but not to the extent seen in sources with older detached shells. In the case of U Cam, however, HCN emission is detected from both the attached envelope and detached shell, whereas HCN emission in R Scl is confined to the former.

For the detached shell to be undetected in HCN, its HCN abundance there must be dramatically lower than in the attached envelope. Adopting the best fit CO model from Lindqvist et al. (in prep.), where the shell is located at $r \approx 11''$ and has a total mass of $\sim 10^{-2}$ $M_\odot$, an upper limit of $f_{\rm HCN} \lesssim 2 \times 10^{-7}$ is obtained. The SEST $J = 1 \rightarrow 0$ data provide the best constraint on this value since a higher HCN abundance in the detached shell would produce more emission in the line wings ($|V - V_\star| \gtrsim 11$ km s^{-1}) than what is observed. From the ATCA data alone, we obtain an upper limit of $f_{\rm HCN} \lesssim 1 \times 10^{-6}$ in the detached shell. The most plausible explanation is the rapid photodissociation of HCN to form CN as the envelope expands away from the star. The difficulty in detecting HCN from sources with larger detached shells (e.g., S Sct, U Ant, and TT Cyg) is consistent with this hypothesis (Olofsson et al. 1996). A more extended distribution of CN as compared to HCN has been directly observed in circumstellar envelopes around IRC+10216 (Dayal & Bieging 1995), U Cam (Lindqvist et al. 1996), and LP And (Lindqvist et al. 2000). Lindqvist et al. (2000) show how this phenomenon can be accounted for by a simple photodissociation model.

6. Conclusions

We have presented interferometric observations of HCN $J = 1 \rightarrow 0$ emission around R Scl that reveal a compact central source with *FWHM* of $1''$, although the data do not sample small enough scales to distinguish a Gaussian from, e.g., a disk or an optically thin sphere. We see no clear indication that the source structure varies with velocity, as would be expected from an expanding spherical shell, but such variations would be difficult to discern because the source is only moderately resolved, and because of the hyperfine structure of the HCN line. Our interferometric data recover, to within the calibration uncertainties, all of the single-dish flux observed with the SEST.

The compact HCN morphology and the narrow line profile of the higher-transition HCN lines indicate that the HCN emission is associated with the present mass loss wind. We estimate a mass loss rate of 2×10^{-7} $M_\odot$ yr^{-1}, significantly less than that needed to account for the detached shell inferred from single-dish CO data. This supports the idea that the star has undergone a recent (within $\sim 10^3$ yr) episode of intense mass loss. The low HCN abundance in the detached shell, which we estimate to be $f_{\rm HCN} \lesssim 2 \times 10^{-7}$, is consistent with the rapid photodissociation of HCN into CN as it expands away from the star.

Modelling the present mass loss envelope using a detailed radiative transfer code, the ATCA data suggest an HCN abundance and envelope size of 4.5×10^{-5} and 5.5×10^{15} cm, respectively. However, such a model cannot be reconciled with single-dish observations of higher J transitions. The single-dish constraints are much better met using an HCN abundance of 1.2×10^{-5} and an HCN envelope size of 1.4×10^{16} cm. The discrepancy may be due to some limitation in the observational data, or to deviations from the adopted circumstellar model with regards to geometry, velocity law, clumpiness, or radiative excitation. However, it is not possible within the adopted circumstellar model to reconcile the interferometer and single-dish data by just changing the mass loss rate.

These observations demonstrate the imaging potential of the Australia Telescope at millimetre wavelengths, even at this early stage in the system development. Future high-resolution observations of CN and CO emission from this object, which are likely to reveal a detached shell morphology, are eagerly anticipated. Such observations could be conducted with the fully upgraded ATCA and, at higher transitions, with the soon-to-be completed Sub-Millimeter Array (SMA).

Acknowledgements. We thank the many ATNF staff that made these observations possible through their hard work on the ATCA upgrade. Special thanks to M. Kesteven for helping to diagnose and correct the phase errors. We also thank S. J. Curran for help with some of the observations. We are also grateful to J. H. Bieging for providing us with his HHT observations. TW is supported by a Bolton Fellowship at the ATNF. FLS, ML and HO acknowledge financial support from The Swedish Research Council. FLS further acknowledges support from the Netherlands Organization for Scientific Research (NWO) grant 614.041.004.

References

Bernes, C. 1979, A&A, 73, 67
Bieging, J. H. 2001, ApJ, 549, L125
Dayal, A., & Bieging, J. H. 1995, ApJ, 439, 996
González Delgado, D., Olofsson, H., Schwarz, H. E., Eriksson, K., & Gustafsson, B. 2001, A&A, 372, 885

González Delgado, D., Olofsson, H., Schwarz, H. E., et al. 2003, A&A, 399, 1021
Gustafsson, B., Eriksson, K., Kiselman, D., Olander, N., & Olofsson, H. 1997, A&A, 318, 535
Kutner, M. L., & Ulich, B. L. 1981, ApJ, 250, 341
Le Bertre, T. 1997, A&A, 324, 1059
Lindqvist, M., Lucas, R., Olofsson, H., et al. 1996, A&A, 305, L57
Lindqvist, M., Olofsson, H., Lucas, R., et al. 1999, A&A, 351, L1
Lindqvist, M., Schöier, F. L., Lucas, R., & Olofsson, H. 2000, A&A, 361, 1036
Mamon, G. A., Glassgold, A. E., & Huggins, P. J. 1988, ApJ, 328, 797
Olofsson, H., Bergman, P., Eriksson, K., & Gustafsson, B. 1996, A&A, 311, 587
Olofsson, H., Bergman, P., Lucas, R., et al. 1998, A&A, 330, L1
Olofsson, H., Bergman, P., Lucas, R., et al. 2000, A&A, 353, 583
Olofsson, H., Carlstrom, U., Eriksson, K., Gustafsson, B., & Willson, L. A. 1990, A&A, 230, L13
Olofsson, H., Eriksson, K., Gustafsson, B., & Carlstroem, U. 1993, ApJS, 87, 305
Schöier, F. L. 2000, Ph.D. Thesis, Stockholm University, Sweden
Schöier, F. L., & Olofsson, H. 2001, A&A, 368, 969
van Zadelhoff, G.-J., Dullemond, C. P., van der Tak, F. F. S., et al. 2002, A&A, 395, 373
Wallerstein, G., & Knapp, G. R. 1998, ARA&A, 36, 369
Willems, F. J., & de Jong, T. 1988, A&A, 196, 173